Laboratory experiments on the breakup of liquid metal diapirs

Jean-Baptiste Wacheul, Michael Le Bars, Julien Monteux, Jonathan M. Aurnou

▶ To cite this version:

Jean-Baptiste Wacheul, Michael Le Bars, Julien Monteux, Jonathan M. Aurnou. Laboratory experiments on the breakup of liquid metal diapirs. Earth and Planetary Science Letters, 2014, 403, pp.236-245. 10.1016/j.epsl.2014.06.044 . hal-01636076

Laboratory experiments on the breakup of liquid metal diapirs

Jean-Baptiste Wacheul[a,b], Michael Le Bars[a,c], Julien Monteux[d], Jonathan M. Aurnou[a]

[a]*SpinLab, Department of Earth and Space Sciences, University of California, Los Angeles, CA 90095-1567, USA*
[b]*Ecole Normale Supérieure, Paris, France*
[c]*CNRS, Aix-Marseille Université, IRPHE UMR 7342, Marseille, France*
[d]*Université de Nantes, CNRS, LPGNantes UMR 6112, France*

Abstract

The validity of the iron rain scenario, *i.e* the widely accepted model for the dynamics of iron sedimentation through a magma ocean during the latest stage of the Earth's accretion, is explored via a suite of laboratory experiments. Liquid gallium and mixtures of water and glycerol are used as analogs of the iron and the molten silicate respectively. This allows us to investigate the effects of the viscosity ratio between iron and silicate and to reproduce the relevant effects of surface tension on the fragmentation dynamics. While the classical iron rain scenario considers a population of purely spherical drops with a single characteristic radius that fall towards the bottom of the magma ocean at a unique velocity without any further change, our experiments exhibit a variety of stable shapes for **liquid metal** drops, a large distribution of sizes and velocities, and an intense internal dynamics within the cloud with the superimposition of further fragmentations and merging events. The relatively complex dynamics we find in our liquid metal experiments will likely have interesting consequences when interpreted into state of the art thermochemical equilibration models.

Keywords: metal diapir, breakup, core formation, magma ocean, metal-silicate equilibration, laboratory experiments

---

1. Introduction

Differentiation of Earth into a core and a mantle was likely completed within the first tens million years after its accretion [e.g. 1, 2, 3]. Numerical simulations [4] and geochemical data on meteorites [5] also show that small planetesimals could have differentiated even earlier when accounting for heating by decay of short-lived radionuclides. There is also strong evidence that the Earth's late accretion is due to collisions with large planetesimals (a tenth to a third of Earth mass), when both the impactor and the proto-Earth were already differentiated [6]. **During accretion**, the Earth and other planets in formation underwent several mechanisms of heating : 1) the decay of relatively abundant radioactive elements with short half-life [7, 8], 2) the conversion of gravitational potential energy by viscous forces during differentiation [9, 10, 11], 3) the collisions themselves with the conversion of huge amount of kinetic energy [12, 13, 14, 15], these impacts alone being able to generate a local melting resulting in a shallow magma ocean [16]. In addition, the primitive atmosphere was certainly much more opaque to IR radiation, so the effect of thermal blanketing was highly efficient [17]. Thus, according to the simulations, Earth has probably had one or several episodes of global magma ocean, with a depth up to thousands of kilometers [18]. In this context, further impacts of differentiated planetesimals would require, for the core of the Earth and the core of the meteorites to merge, that the

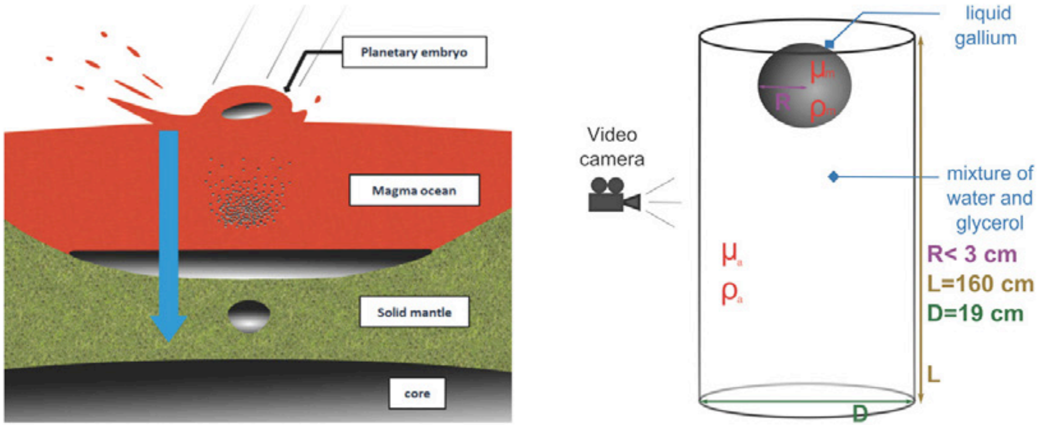

Figure 1: Left: schematic of the metal/silicate separation after the impact of a differentiated planetesimal with the early Earth in reference to the work of [1]. The equilibration by diffusion between the impactor's core and the magma ocean during the metal rainfall and later when sinking through the solid mantle as a large diapir are poorly constrained, and strongly depends on the fluid dynamics of the iron sedimentation. Right: schematic of our experiment.

latter flows through the magma ocean (Fig. 1). This process can be seen as a secondary step of mixing between core and mantle, since it could lead to partial or complete thermo-chemical equilibration between the sinking metal and the molten surrounding silicates, depending on the characteristics of the flow of the core material through the mantle.

The importance of this exchange is an issue for the interpretation of numerous geochemical proxies, such as the Tungsten 182 signal. Hafnium (^{182}Hf) disintegrates in Tungsten (^{182}W) with a relatively short half-life of 9 My, comparable with the time scale of core differentiation. They are both refractory but Tungsten is siderophile whereas Hafnium is lithophile. This is why the radioactivity ^{182}Hf-^{182}W has been used in multiple studies to approximate the age of terrestrial bodies' core [19, 20, 21]. However due to the late impacts and possible mixing that could occur, there are very poor constraints on which event – late impacts or core differentiation – is relevant for the interpretation of the ratio ^{182}W/^{184}W. Then the age given by this proxy could be any intermediary between **the initial differentiation of the proto-Earth** and the most recent giant impact that it endured, depending on how much ^{182}W has been absorbed by the asteroid's core during its passing through the mantle [21]. The same kind of interrogation can be held against interpretations of the U/Pb proxy, and for the coefficients of partition between metal and silicate. Finally, that indetermination concerns every equilibration by diffusion such as diffusion of heat and diffusion of momentum by viscosity, both leading to indetermination on the initial thermal state of the mantle and the core, and on the repartition of the energy between these two [10, 22]. Thus, in order to model the evolution of both Earth's core and mantle, it is important to understand **the fluid dynamics at the drop scale during the iron sedimentation** [23].

2. Parameters controlling the fluid dynamics of the iron sedimentation

The equilibration between the iron and molten silicate strongly depends on the typical size of the metal entities**. Indeed**, for a given volume of metal, a single large diapir would fall rapidly through the magma ocean with a relatively small surface of exchanges, while the fragmentation of the same volume of iron through a large number of small structures broadens the surface **area** of exchanges and slows down the falling velocity, hence **extending** the time during which iron and silicate equilibrate. **Note that in the present paper, we generically use the term diapir, classically used in geology to designate large liquid intrusion into surrounding rocks driven by buoyancy forces, to designate any large blob of liquid metal moving through a more viscous but less dense environment**.

Several approaches have been developed in order to give a physically coherent description of what happens when a liquid iron diapir falls through a magma ocean, and ultimately to provide a time scale for the equilibration. At first order, the shape of the falling diapir is dominated by two forces. The surface tension tends to stabilize a spherical shape, while the dynamic pressure deforms the diapir and tears it apart. Let us assume for instance, a typical diapir with a radius $R_0 = 10$ km falling at the inviscid, free fall Newtonian velocity valid for a rigid sphere

$$V \simeq \sqrt{\frac{\Delta\rho}{\rho_a} g R_0}, \tag{1}$$

where ρ_a is the silicate density ("a" standing for "ambient"), $\Delta\rho$ the density difference between iron and silicate, and g the gravity. Assuming that the Earth has already more than half its final mass, V is close to 1 km/s and the Reynolds number of the flow in the mantle, which represents the ratio between inertial and viscous forces in the Navier-Stokes equations

$$Re_a = \frac{\rho_a V R_0}{\mu_a}, \tag{2}$$

where μ_a is the silicate dynamic viscosity, is above 10^{10}. This huge Re value provides an *a posteriori* validation of the velocity estimated by Equation (1). It also implies that dynamic pressure scales as the inertia. On the other hand, the characteristic strength of surface tension is directly linked to the radius of curvature of the surface, so its order of magnitude roughly depends on the radius of the spheroid diapir R_0. A good estimation of the stability of a diapir is given by the Weber number, which is the ratio of inertia over surface tension:

$$We_a = \frac{\rho_a V^2 R_0}{\sigma}, \tag{3}$$

where σ is the coefficient of surface tension. For $We \gg 1$, diapirs are unstable and break-up. Below some threshold of order 1 (e.g. $We_c = 6$ for rain drops, see [24]), surface tension and inertia compensate, and the diapir is stable. This widely used breakup criterium [e.g. 16, 25, 26, 27] allows **a calculation of the** maximal radius for stable diapirs, given some hypothesis regarding its falling speed. For the simple Newtonian velocity scaling given by (1), the maximal radius corresponds to

$$R_{cap} = \sqrt{We_c \frac{\sigma}{\Delta\rho g}}, \tag{4}$$

which is about 1 to 2 cm for the Earth's iron/silicate system. Such a criterium is well known in the case of water drops in the air, for which it has been confirmed by experiments [24]. It has also been supported by a recent numerical study designed for the case of an iron diapir in molten silicate [11]. In this study, the initial spherical diapir flattens, then breaks up within a distance of no more than 10 diapir radii, and the diapir's sons continue to break up, cascading downward to the scale R_{cap} where surface tension compensates the pressure forces. However, in these axisymmetric simulations, the breakup is not actually modeled, but is supposed to occur shortly after the topological change from pancake to torus, so the size of the resulting drops remains unknown. According to this scenario, there is no way for a 10 km radius diapir corresponding to a Weber number above 10^{14} to remain entirely intact during its fall. It should rapidly break up into a cloud of drops of radius R_{cap}, *i.e.* the so-called “iron rain”. Then, most models of metal-silicate equilibration [e.g. 11, 25, 28] assume that all iron drops have an identical and fixed spherical shape with a radius equal to R_{cap} and a unique sedimentation velocity based on free fall models.

On the other hand, for diapirs with a radius of 10 km and above, the Weber number is so large (above 10^{14}) that its dynamics are controlled by the inertia of the flow only, allowing to completely ignore the effects of surface tension. The resulting immiscible models lead to interesting findings, although they are very dependent on the type of assumption made to build them. Deguen et al. [27] supposed that the diapir rapidly becomes a cloud of drops that then evolves in a coherent manner as a buoyant thermal, whose radius grows linearly with depth because of turbulent mixing with the outside. They found that for a shallow magma pond created by an impact as for a deep magma ocean [29], there should be enough dilution between metal and silicate for them to equilibrate. On the contrary, Dahl and Stevenson [26] considered a diapir with an almost constant shape eroded by Raleigh-Taylor and Kelvin Helmholtz instabilities. The conclusion was then very different because the dilution was in that case insufficient to drive a full equilibration for diapirs with a radius above 10 km.

Open questions thus remain on all stages of the iron sedimentation, from the large-scale dynamics to the behavior at the smallest scales, where surface tension modifies the modalities of diffusive exchanges. In this context, the numerical study [30], in agreement with the results for water drops in the air [24], pointed out that the cloud of drops contains a whole distribution of sizes and not just a single one [31]. Furthermore, the distribution of speeds and the relation between size and speed of drops are not trivial, supporting the idea that the iron rain scenario with a single size and speed may be inaccurate. However, the conclusions of [30] are supported mostly by 2D numerical simulations, where surface tension is not properly rendered. Hence they still need confirmation.

In addition, it is worth noting that all previous studies of the stability of diapirs have neglected the influence of the viscosity ratio between the ambient fluid and the metal

$$r_\mu = \frac{\mu_a}{\mu_m}. \tag{5}$$

However, when the magma cools down, or as the diapir goes deeper into the mantle, the magma becomes closer to the solidus and contains more crystals. Therefore, the viscosity of the magma is expected to increase from 10^{-3} to 10^2 Pa.s, corresponding to r_μ ranging from 1 to 10^5. Such a large viscosity ratio is known to have a significant effect on the shape of falling drops [e.g. 32, 33]. Indeed, from the continuity of the velocity and the stress tensor at the drop interface, a large r_μ in a large Reynolds number flow implies intense internal recirculations inside the drop, which then deforms and may be dynamically stabilized. This has not been investigated in a geophysical context.

Here we report the first experiments designed to simulate the last stages of the fragmentation process with realistic values of the iron/silicate viscosity ratio and relevant behaviors regarding the effects of surface tension on the fragmentation dynamics. The set-up is presented in section 3. In section 4, we investigate the variety of stable shapes for iron drops, as well as their mutual interactions and proper dynamics after the initial breakup. The measured distributions of size and velocity are presented in section 5 and 6, highlighting the influence of the viscosity ratio. The relevance of the complex fluid dynamics shown by our experiments to the Earth is illustrated in section 7 by a simple equilibration model based on our results. Conclusions and open questions are given in section 8.

3. Set-up and methods

Our experimental set-up is sketched in Fig. 1. As an analogue for the magma ocean, we use a 160 cm high cylindrical tank, with a diameter of 19 cm, filled with a mixture of water and glycerol. The glycerol (resp. water) has a dynamic viscosity of 1.08 Pa.s (resp. 0.00093 Pa.s) at room temperature (23^oC): the mixture of the two allows us to explore a range of 3 orders of magnitude for the viscosity of the ambient fluid μ_a, with a density ranging from $\rho_a = 1260$ kg.m^{-3} for pure glycerol to $\rho_a = 997$ kg.m^{-3} for pure water. As an analogue for the liquid iron diapir, we use liquid gallium. It has a viscosity $\mu_m = 1.9.10^{-3}$ Pa.s and a density $\rho_m = 6095$ kg.m^{-3}. The gallium is initially contained in a latex balloon at the top of the set-up; the ballon is then popped by a syringe needle at the beginning of the experiment. This method has two advantages: the amount of gallium is precisely known by **weighing** the balloon, and since the retraction of the balloon occurs within about 1/50 second, the diapir has no initial speed and its initial shape is the one imposed by the balloon. The fall of the diapir is then recorded by a high

Symbol	Parameter	Value for the Earth	Value in our experiment
ρ_a	ambient fluid density	3000 kg.m^{-3}	997 – 1260 kg.m^{-3}
ρ_m	liquid metal density	7000 kg.m^{-3}	6095 kg.m^{-3}
μ_a	ambient fluid viscosity	10^{-3} – 10^{2} Pa.s	10^{-3} – 10^{0} Pa.s
μ_m	liquid metal viscosity	10^{-3} Pa.s	1.9.10^{-3} Pa.s
r_μ	viscosity ratio	1 to 10^5	0.5 to 500
σ	surface tension	1 J.m^{-2}	0.7 J.m^{-2}

Table 1: List of relevant parameters and typical Earth's and experimental values.

speed USB camera at 136 frames per second, with a resolution of 196x1280 pixels. In addition to this camera, higher resolution videos of the lower part of the experiment are taken at 60 frames per second with a resolution of 1280x720 pixels. Beyond direct visualization, the videos are used to recover the shape and velocity of the droplets, after removing the background and after binarization. Each droplet in a selected frame is detected using the Matlab Image Processing toolbox, and an equivalent radius is retrieved by measuring its apparent area A and applying the formula $r = \sqrt{A/4\pi}$. This is a lower estimate since the drops are oblate at different degrees. We also construct space-time diagrams by extracting the same horizontal line from all frames of a chosen video. The resulting image then gives us the horizontal radius of each droplet reaching the selected depth as well as its arrival time, hence its mean fall velocity.

Relevant parameters are listed in table 1 in comparison with Earth's values. Experiments were run with 6 different sizes of the initial diapir ranging from an equivalent radius of 14 mm to 30 mm, and with 4 viscosities of the ambient fluid 0.001, 0.01, 0.1 and 1 Pa.s. In the inertial regime, the characteristic velocity of the flow scales as the Newtonian velocity introduced in Equation (1). Then, the dynamics is entirely characterized by 4 dimensionless parameters: the density ratio $\Delta\rho/\rho_a$, the viscosity ratio $r_\mu = \mu_a/\mu_m$, and the Newtonian Reynolds and Weber numbers Re_a and We_a **(based on the Newtonian velocity)**. In our experiment, $\Delta\rho/\rho_a$ remains almost constant at about 5 (the ambient density only marginally varies with the proportion of water), which means that as in the geophysical setting, density changes are of order 1 (*i.e* no Boussinesq approximation). With the accessible range of initial diapir radii, we are able to produce Reynolds numbers from 10 to 4×10^4 and Newtonian Weber number from 14 to 64. As shown in Fig. 2, this is obviously limited compared to the possible geophysical values, especially for diapirs with large initial radius. But even if the dynamic similitude between the experiment and reality is not exact, the experiment are capable of reaching the relevant dynamical regime, with a fully turbulent flow and a Weber number above the critical value for breakup. Furthermore, the similitude is exact for diapir radii around the decimeter scale, hence for the final stages of the real iron rain. Note finally that our experiment is the first one to take into account the effects of the viscosity ratio, which spans the range $0.5 - 500$ in our set-up.

4. Zoology of the breakup

The results of 3 experiments in pure glycerol with different initial radius of the diapir are shown in figs. 3A, 3B and 4. Fig. 5 shows a closer look of the various possible shapes of gallium drops obtained in the experiment presented in Fig. 4. According to the classical iron rain scenario applied to our

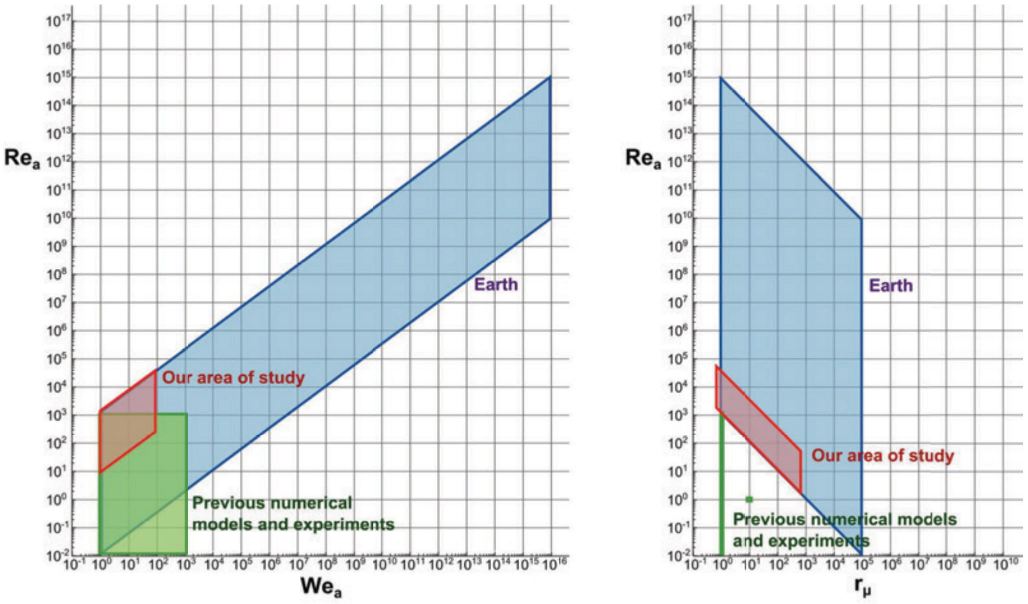

Figure 2: In blue, area of the parameters space associated with the fall of iron diapirs in the context of Earth's accretion. Variations are due to changes in the viscosity of the magma ocean and in the diapir initial radius. For comparison, the area explored by previous studies [11, 29, 30] is shown in green, whereas the parameter space explored by the present study is shown in red.

experimental set-up, any diapir with a Weber number larger than 6 should rapidly give rise to a cloud of spherical drops with a single characteristic radius $R_{cap} = 1$ cm that should fall with a Newtonian velocity $V = 74$ cm/s, without any further dynamical change. This is not the case.

For the lowest initial radius (Fig. 3A), the diapir is stable even if its Weber number is above the known threshold 6 **(note that the effective Weber number calculated using the measured falling velocity instead of the scaling given by Equation (1) is 9)**. One can also notice that its equilibrium shape is not spherical: the drop takes the form of a cap, where the intense internal recirculation driven by viscous coupling with the outside stabilizes its shape (see also the sketch in Fig. 5B). The viscosity ratio strongly influences the shape and the condition for stability of a single structure, as studied more precisely by [32, 33] using axisymmetric numerical simulations. There is a clear tendency for large viscosity ratios to stabilize the drops, and the diapir shown in Fig. 3A is indeed unstable for r_μ below 50 **(not shown here)**. According to results in [32, 33], which are coherent with our experimental observations, the critical Weber number can actually be more than one order of magnitude larger than the classically used value $We_c = 6$, depending on the viscosity ratio and the initial shape of the drop.

The slightly larger diapir shown in Fig. 3B rapidly breaks up into three large caps plus some smaller drops. A striking point here is that after this initial break-up, the dynamics is not frozen: the three caps interact and two of them finally merge to re-build a larger diapir. For comparison, the same experiment but with an ambient viscosity 100 times less viscous is shown in Fig. 3C. The initial behavior of the diapir is similar but the breakup

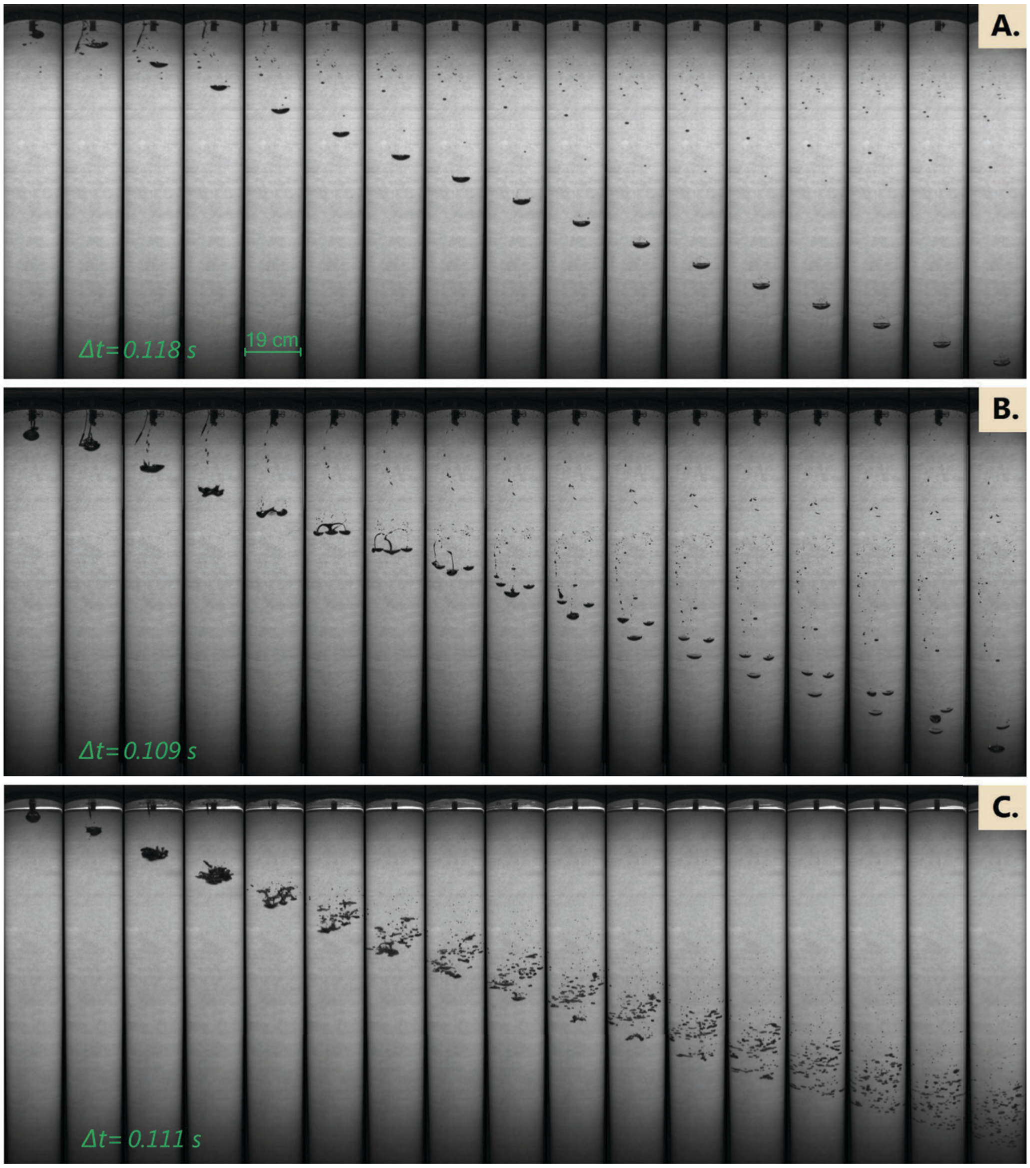

Figure 3: Successive snapshots with a fixed time interval for 3 experiments. A : Fall of a 14 mm initial radius diapir in pure glycerine, corresponding to $Re_a = 12$, $We_a = 14$ and a viscosity ratio of 500. The diapir has a stable cap shape. B : same as A but for a 23 mm initial radius diapir, corresponding to $Re_a = 24$ and $We_a = 37$. The diapir breaks up in 3 main cap-shaped stable drops of close sizes. C : same as B but for an ambient fluid 100 **times** less viscous, corresponding to $Re_a = 2400$, $We_a = 37$ and a viscosity ratio of 5.

Figure 4: Successive snapshots with a fixed time interval $\Delta t = 0.18s$ for a 30 mm initial radius diapir falling through pure glycerol, corresponding to $Re_a = 37$, $We_a = 64$ and a viscosity ratio of 500. One can notice that the mean speed of the front of the diapir is rather constant.

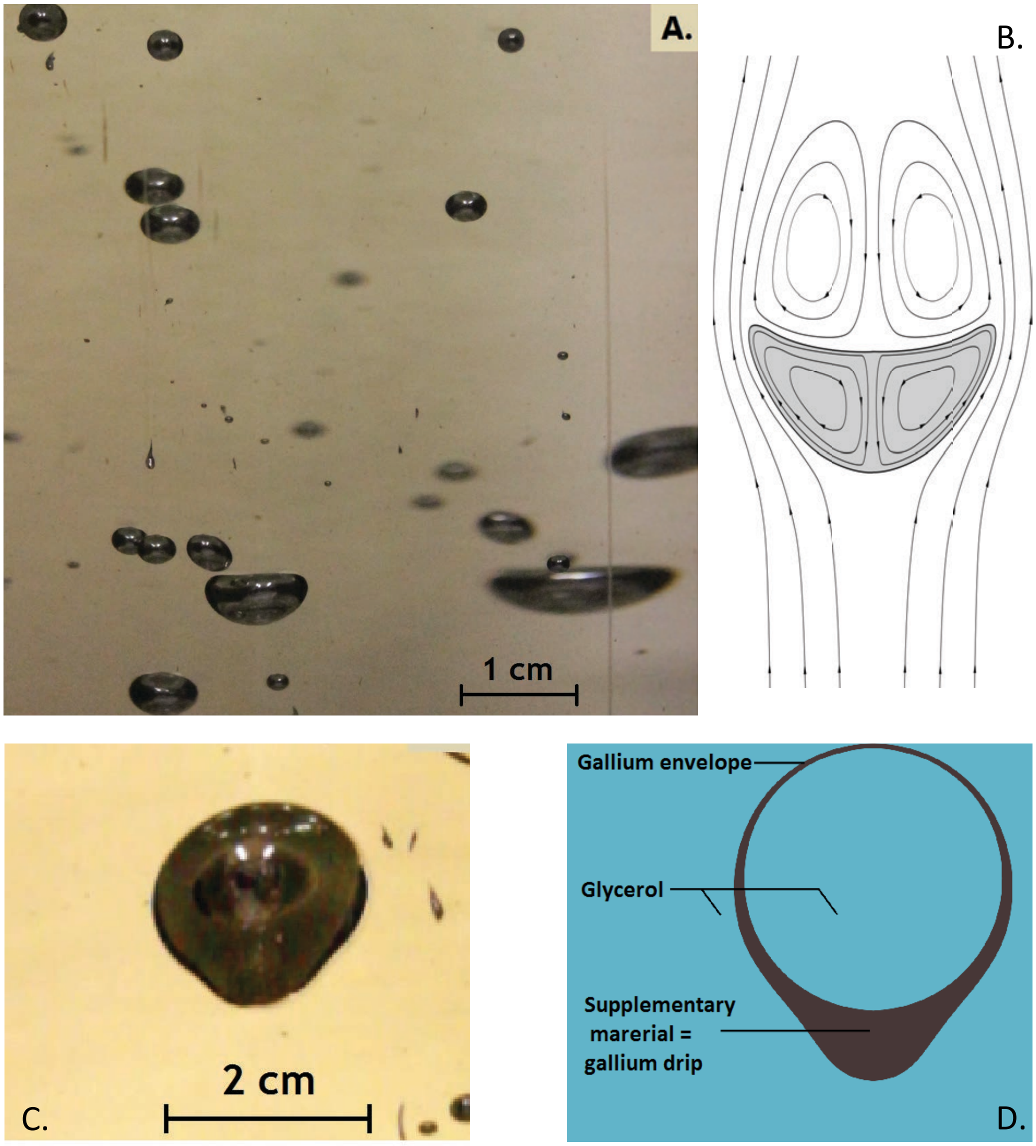

Figure 5: A: drops of liquid gallium of various sizes falling through pure glycerol. Several intermediates between cap shape and spherical shape are present. B: expected streamlines of the relative flow within and around a falling diapir with a cap shape (shown in gray). C: gallium bubble enclosing glycerol formed during the breakup of a 30 mm radius diapir in pure glycerol. Due to its reduced buoyancy compared to full gallium drops, it falls slowly. These structures last from one tenth of **a** second to several minutes. D: schematic of a gallium bubble.

dynamics is clearly different, even if the Weber number is the same in both experiments. The Reynolds number is greater in 3C because of the smaller ambient viscosity; but comparing both series of pictures, one can notice that the falling velocities are close in the two experiments: both cases are clearly in the Newtonian regime, and changes in Re_a cannot explain changes in the fragmentation behavior. We expect this to be due to the viscosity ratio, which allows the dynamical stabilization of large drops by internal recirculation in case **3**B.

The dynamics of initially large diapirs systematically follows the series of stages illustrated in Fig. 4: after a short acceleration, we observe waves forming on the surface of the diapir, qualitatively similar to the description of [26]. But almost simultaneously, the diapir flattens as the waves amplitude rises: it evolves towards a thin wavy sheet where the axisymmetry is fully broken. It breaks up shortly after this stage: holes appear in the sheet, the transient ligaments retract and break-up. The drops resulting from this burst have various sizes and shapes, and the biggest ones continue to break up in the same way until a steady-state is reached. The whole process can be seen as a downward cascade toward small scales where surface tension is important. However, we also observe multiple coalescence of droplets several times in a row, corresponding to a non-linear inverse cascading process. From the video, we see that small drops accelerate and merge when they are near bigger drops whose rear recirculation **engulfs** them. One can argue that the narrowness of our experiment limits the spreading of the metallic droplet cloud, thereby enhancing the typical frequency of droplet collisions. But as noted above, coalescence happens even if there are very few drops. We thus believe that this inverse cascade process is also relevant in larger domains, as for instance in magma oceans.

Fig. 5A shows a closer instantaneous view of the drops cloud once the steady-state is reached. A whole distribution of shapes and sizes is observed. Large drops have a cap shape stabilized by internal recirculation (see Fig. 5B), and the smallest drops adopt a spherical shape; a continuity of flattened ellipsoidal shapes is observed in between. We have also observed a novel metastable structure (Fig. 5C) formed during the breakup of the biggest diapirs. These structures look like a hot air balloon and fall slowly relative to other droplets of comparable size. From slow motion videos of their formation and disappearance, it turns out that they are thin bubbles of gallium enclosing glycerol, similar to bubbles of soapy water in the air (see Fig. 5D): this explains their relative stability as well as their anomalously low settling velocities for their rather large size.

5. Distribution of sizes and influence of the viscosity ratio

Fig. 6 shows the cumulative distribution **of droplets sized obtained from the breakup of the largest class of diapir for** a viscosity ratio of $r_\mu = 50$. This corresponds to $Re_a = 368$ and $We_a = 64$. Taking into account the resolution of the video (176 pixels for 19.6 cm), we are able to detect the size of drops larger than 0.6 mm in radius, the smaller ones being detected as drops of 0.6 mm. In agreement with the simulations of [30], the breakup of metal diapirs does not create droplets of one single size but a whole distribution of equivalent radii. Because the formation of drops results from the generic process of ligament rupture, their size distribution is well

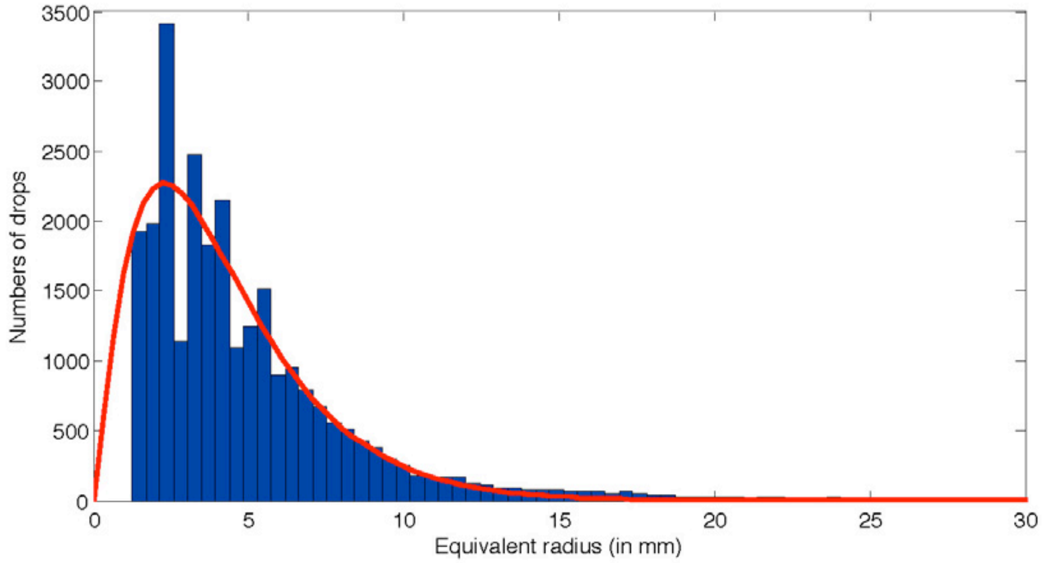

Figure 6: Histogram of the equivalent radius of the droplets created by the breakup of a 30 mm initial radius diapir falling through a mixture of glycerol and water (in blue) and best fitting Gamma distribution (in red, with shape 2.2 and scale 1.9). Dimensionless parameters of the experiment are $Re_a = 368$, $We_a = 64$ and $r_\mu = 50$. The low cutoff radius is set by the resolution of the video to 0.6 mm. **A large number of measurements are necessary for obtaining converged statistics. This cumulative distribution was thus constructed from 6 runs of the same experiment and using the last 10 frames of each video, i.e. once a statistically steady state is reached and before the fastest droplet touches the bottom of the tank.**

fitted by a Gamma function, similar to the one obtained in the case of water drops in the air [24]. Note however that in this last case, the viscosity ratio is reverse (*i.e* the more viscous fluid is inside) and the shapes of the obtained drops are very different. Our distribution is tightened around a mean radius of 4 mm. This value can be related to a breakup criterion, now understood in a statistical sense: surface tension sets the characteristic length scale of the distribution, the mean radius. Using our experimental results, the critical Weber number corresponding to this radius is $We_c = 1$. The distributions obtained for diapirs with different initial sizes are similar to the one shown in Fig. 6, and so is the measured mean radius, provided that these diapirs are large enough to create a distribution of sizes that converges statistically. This condition is verified for the 4 biggest classes of diapirs that we have produced.

Fig. 7 shows series of snapshots from 4 experiments with the same initial diapir but different viscosity ratios. With our present set-up, because a large number of drops superimposes on the video, it was not possible to detect automatically their contour for a viscosity ratio smaller than 50**. Hence we could not** perform a systematic quantitative study of the sizes distribution as a function of r_μ. But relying on direct observation, we see that as already noticed in section 4 for single structures, there is a clear tendency for large viscosity ratios to stabilize bigger drops. In all cases, we expect to systematically recover a Gamma-type distribution for the equivalent radii. This means that the distributions always have the same shape, with a peak at a small scale corresponding to $We_c = 1$, and an exponential tail. But we expect the slope of this tail to be significantly more gentle when the viscosity

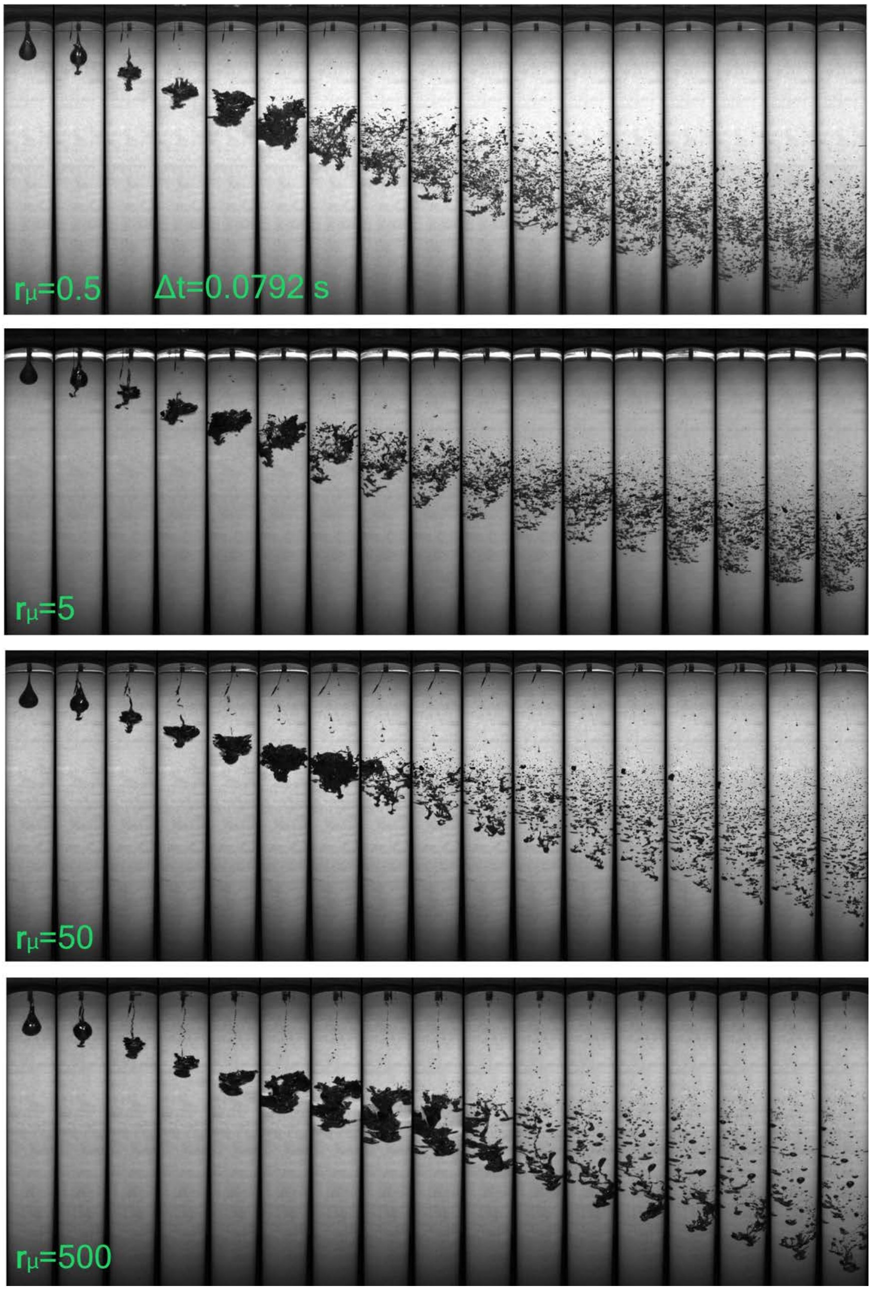

Figure 7: Series of snapshots of the diapirs evolution for 4 runs of the experiment with a 31 mm initial radius diapir. From top to bottom, only the viscosity of the ambient fluid increases; the corresponding viscosity ratios are 0.5, 5, 50, and 500. **Rigorously, changing the ambient viscosity also changes the Reynolds number. But it may be noticed from the snapshots that the mean sedimentation velocities in the 4 cases are close, hence mostly independent of the viscosity, as expected in the Newtonian limit. We thus argue that the various observed dynamics are primarily related to changes in the viscosity ratio.**

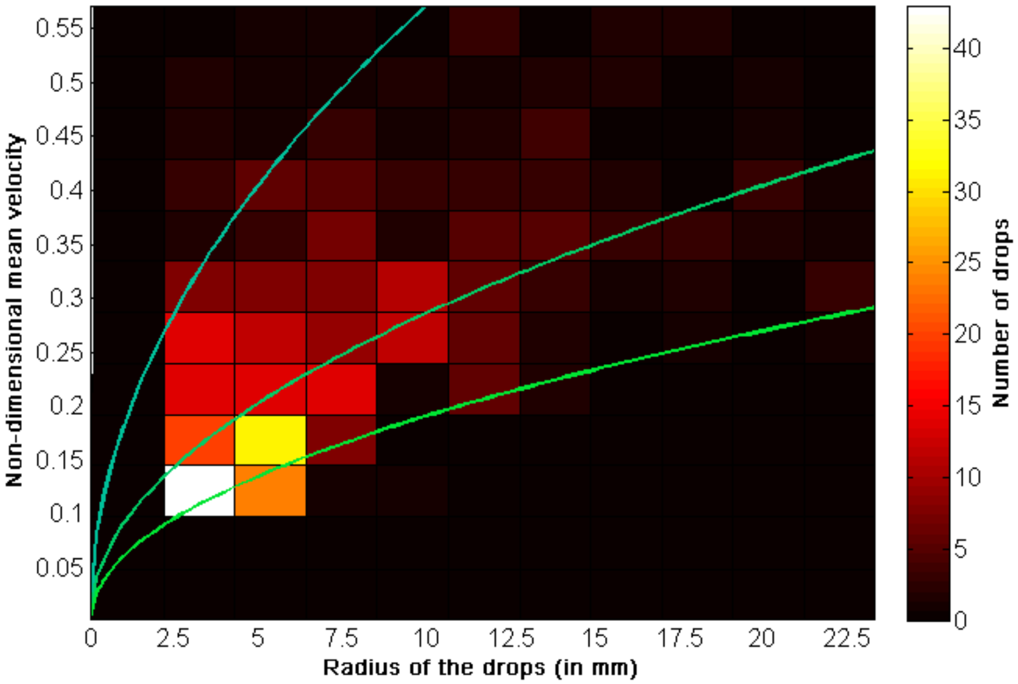

Figure 8: Distribution of the drops equivalent radii (in mm, along the x-axis) and speeds (non-dimensionnalized by the Newtonian speed of the initial diapir, along the y-axis). The initial radius of the diapir is 23 mm and the viscosity ratio is 50, which gives $Re_a = 244$ and $We_a = 37$. Three curves of the corresponding Newtonian velocity scaling (1) with a prefactor respectively equal to 1, 1/2 and 1/3 from top to bottom, are shown in green.

ratio increases. This corresponds to a decreasing value of the "shape" of the Gamma function: for instance, [24] found a shape value of 4 for the breakup of water in the air (viscosity ratio 2×10^{-2}), while we find a shape of 2.2 for a viscosity ratio of 50, as shown in Fig. 6.

6. Simultaneous distributions of sizes and velocities

The interactions between the droplets lead to a wide range of sizes and velocities in our experiments. Fig. 8 shows the distribution of sizes and speeds for a viscosity ratio $r_\mu = 50$ and a diapir with an initial radius of 23 mm, using the values obtained from a space-time diagram at a distance of 140 cm from the initial position of the center of mass of the diapir. It is plotted in the same way as in [30]. The fact that velocities are calculated from the travel time through the tank integrates a large part of the variability due to raw turbulence and allows talking about the mean structure of the flow. Interestingly, the drops' velocities do not follow a fixed Newtonian scaling, even when adjusting the pre-factor. This result seems to validate the entrainment hypothesis described by Deguen et al. [27, 29]: after the breakup, the drops fall as an interacting cloud whose velocity is determined by the inertia of the whole flow, related to the initial mass of the diapir. Additional fluctuations are related to the turbulent mixing and interactions between drops.

7. Typical equilibration length

We can estimate a rough length scale of equilibration following the same reasoning as in [11], but using the distribution of sizes and velocities found in our experiments. Note that the preliminary equilibration models shown below are meant only for illustration of potential consequences of the complex dynamics exhibited in our experiments. The question of equilibration clearly deserves more complete studies.

In our simple model, we neglect the breakup distance and consider that the distribution of sizes and speeds has reached a steady state. From simulations [11], from previous experiments [29] and from our observations, breakup occurs within a typical length scale of a few initial radii, so the previous hypothesis is valid for initial entities at least 10 times smaller than the mantle depth: we choose here an initial diapir of radius 10 km **sedimenting in a magma ocean with a minimum depth of** 100 **km.** We suppose that the metal concentration C_m in a chemical element of interest (e.g., Ni, Co,W, Hf) is uniform inside each drop and that it evolves following a simple Fick's law

$$\frac{4\pi}{3} r^3 \frac{dC_m}{dt} = -4\pi r^2 \kappa \frac{C_m - C_{m,eq}}{\delta_{BL}}, \tag{6}$$

where r is the drop radius, κ the chemical diffusivity coefficient of typical order 10^{-8} m^2/s, and $C_{m,eq}$ the equilibrium concentration. We further assume that the thickness of the chemical boundary layer δ_{BL} scales as $\delta_{BL} = \sqrt{2\kappa r/v}$, where v is the local speed of the flow around the droplet, assumed to be constant [see details in 11]. We define the degree of equilibration as

$$C^*(t) = \frac{C_m(t) - C_m(t=0)}{C_{m,eq} - C_m(t=0)}. \tag{7}$$

Equation (6) then leads to an exponential solution

$$C^*(t) = 1 - e^{-t/\tau} \quad \text{where} \quad \tau = \frac{r^{3/2}}{3}\sqrt{\frac{2}{\kappa v}}. \tag{8}$$

Following our experimental results, we evaluate the degree of equilibration using three different values for the local speed of the drops and the speed at which the cloud of drops is entrained. The reference case corresponds to the standard iron rain scenario with a cloud of drops with a uniform radius

R_{cap}, and where the local and global speeds are the corresponding Newtonian speed. **Two other scenarios based on our experimental results are investigated. The local speed is given in one case by the Newtonian speed for each drop whose radius follows a Gamma-distribution, and in the other case by the sizes / speeds distribution found in our experiment and presented in Fig. 8, implicitly assuming that this distribution does not depend on the large scale parameters such as the mean diameter and velocity of the drop cloud. In both cases, the global speed is the Newtonian velocity of the initial** 10 **km radius diapir. This estimate agrees with the present experimental results, as may for instance be observed in figure 7. Note however that the global sedimentation speed probably decreases during sedimentation because of the progressive entrainment of ambient fluid, as shown by [27, 29]. This effect is not seen here, probably because of the limited extension of our container.** Corresponding equilibration results for the three models are shown in Fig. 9.

In all cases, the entire distribution of drops fully equilibrates before reaching the bottom of the magma ocean. However, the predicted depth of equilibration is 1 to 3 orders of magnitude larger when considering the scenarios derived from our fluid mechanics experiments compared to the idealized iron rain. **This is the result of two combined effects highlighted by our laboratory experiments: the drop falling velocities are significantly larger than in the classical iron rain, and the drop size distribution puts a significant fraction of the metal phase in drops larger than** R_{cap}**, which implies a smaller surface of exchange between iron and**

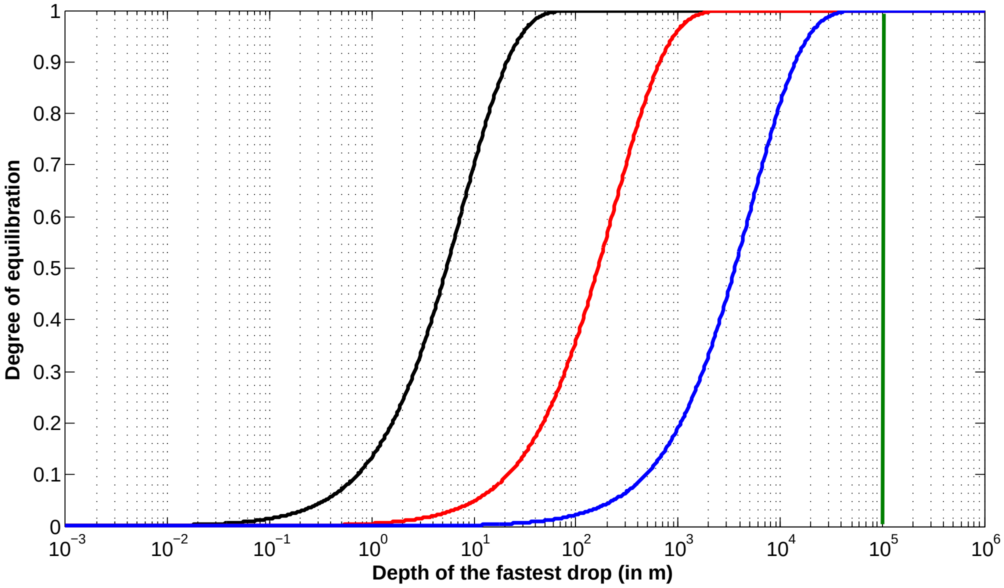

Figure 9: Degree of equilibration of **a cloud of droplets resulting from the fragmentation of** an initially 10km radius diapir **and** falling through a magma ocean. The classical iron rain scenario is shown in black for reference. Two scenarios derived from the statistics of our experiments with an initial radius $R = 30mm$ and $r_\mu = 50$ are also shown, where the global speed of the drop cloud is taken as the Newtonian velocity of the initial 10 km radius diapir. In red, the local speed of the drops is derived from the distributions shown in Fig. 8. In blue, the local speed is given by the Newtonian scaling law for each drop radius. **Note that the present model neglects the breakup distance of the initial diapir. For an initial diapir of radius 10km, this implies a minimum depth of the magma ocean of 100km, shown by the vertical green line.**

silicate. As a result, equilibration will integrate a broader range of conditions regarding pressure and temperature, and the energy and the mass exchanged by diffusion during the fall will be brought much deeper. Besides, for several elements, the partition coefficient depends on the pressure of equilibration. Expected changes in the depth of equilibration will also change their final repartition between core and mantle.

8. Conclusions and open questions

Our laboratory experiments on the fragmentation of gallium drops in glycerol brings a new light on the dynamics of the iron rain that took place at the final stages of the Earth's accretion. We show here that while the classical iron rain scenario considers a population of spherical drops with a single characteristic radius that fall towards the bottom of the magma ocean at a unique velocity without any further change, the fragmentation of an initially large diapir actually gives rise to a variety of stable shapes, a large distribution of sizes and velocities, and an intense internal dynamics within the cloud with the superimposition of further fragmentations and merging. Previous models for chemical and/or thermal equilibration [see e.g. 22, 25] are only true in a statistic mean sense. On the basis of our very simple equilibration model, we still predict a complete equilibration before reaching the core, but at a significantly deeper depth. One should **also** keep in mind that the probability of a "strange" event, *i.e* an anomalously large diapir or an anomalously slow falling velocity, is statistically possible, especially for large viscosity ratios: consequences for the initial state of the Earth would then be significant.

Additional experiments are now necessary to complement the first conclusions drawn here, notably with a larger tank to avoid confinement effects and to allow for initially larger diapirs. Also it now appears necessary to take into account, in more evolved models of equilibration, the complex internal dynamics between drops inside the clouds, including the observed inverse cascade and the global sedimentation dynamics. It is also necessary, in addition to the first study for fixed-shape spherical drops by [28], to account for the very intense internal dynamics inside and outside large drops, which both stabilizes and deforms them, and should increase the equilibration process by advection. All these effects clearly deserve further studies that are beyond the scope of this paper. Finally, our experiments have highlighted the importance of the viscosity ratio on the fluid dynamics of the fragmentation and sedimentation processes. As in Earth, the heat brought by the conversion of gravitational and kinetic energy during accretion is not negligible [**see e.g. 16, 22**], it would now be interesting to study the strong coupling between the heating by viscous damping of the intense flows caused by the fall of iron diapirs, the changes in the ambient viscosity induced by this thermal evolution, and the corresponding **evolution of the drop size distribution**.

Acknowledgments

We thank Prof. E. Villermaux for helpful discussions.

References

[1] D. J. Stevenson, Origin of the Earth, Oxford University Press, 1990, Ch. Fluid dynamics of core formation.

[2] M. Boyet, J. Blichert-Toft, M. Rosing, M. Storey, P. Télouk, F. Albarède, ^{142}Nd evidence for early Earth differentiation, Earth and Planetary Science Letters 214 (2003) 427–442.

[3] M. Boyet, R. W. Carlson, ^{142}Nd evidence for early ($>$ 4.53Ga) global differentiation of the silicate Earth, Science 309 (2005) 576–581.

[4] W. Neumann, D. Breuer, T. Spohn, Differentiation and core formation in accreting planetesimals, Astronomy & Astrophysics 543 (2012) A141.

[5] T. Yoshino, M. Walter, T. Katsura, Core formation in planetesimals triggered by permeable flow, Nature 422 (2003) 154–157.

[6] A. Morbidelli, J. Lunine, D. O'Brien, S. Raymond, K. Walsh, Building terrestrial planets, Annual Review of Earth and Planetary Sciences 40 (2012) 251–275.

[7] R. Merk, D. Breuer, T. Spohn, Numerical modeling of ^{26}Al-induced radioactive melting of asteroids considering accretion, Icarus 159 (2002) 183–191.

[8] M. Walter, R. Tronnes, Early Earth differentiation, Earth and Planetary Science Letters 225 (2004) 253–269.

[9] D. C. Rubie, F. Nimmo, H. J. Melosh, Treatise on Geophysics, Elsevier, 2007, Ch. Formation of Earth's core.

[10] J. Monteux, Y. Ricard, F. Coltice, N. Dubuffet, M. Ulvrová, A model of metal-silicate separation on growing planets, Earth and Planetary Science Letters 287 (2009) 353–362.

[11] H. Samuel, A re-evaluation of metal diapir breakup and equilibration in terrestrial magma oceans, Earth and Planetary Science Letters 313 (2012) 105–114.

[12] V. S. Safronov, The heating of the Earth during its formation, Icarus 33 (1978) 3–12.

[13] W. M. Kaula, Thermal evolution of Earth and moon growing by planetesimal impacts, Journal of Geophysical Research 84 (1979) 999–1008.

[14] C. Reese, V. Solomatov, Fluid dynamics of local martian magma oceans, Icarus 184 (2006) 102–120.

[15] J. Monteux, N. Coltice, F. Dubuffet, Y. Ricard, Thermo-mechanical adjustment after impacts during planetary growth, Geophysical Research Letters 34 (2007) L24201.

[16] B. Tonks, J. Melosh, Core formation by giant impacts, Icarus 100 (1992) 326–346.

[17] Y. Abe, T. Matsui, The formation of an impact-generated H_20 atmosphere and its implications for the thermal history of the Earth, Journal of Geophysical Research 90 (1985) 545–559.

[18] B. Tonks, J. Melosh, Magma ocean formation due to giant impacts, Journal of Geophysical Research 98 (1993) 5319–5333.

[19] D.-C. Lee, A. N. Halliday, Hf-W isotopic evidence for rapid accretion and differentiation in the early solar system, Science 274 (1996) 1876–1879.

[20] C. Harper, S. Jacobsen, Evidence for ^{182}Hf in the early solar system and constraints on the timescale of terrestrial accretion and core formation, Geochimica et Cosmochimica Acta 60 (1996) 1131–1153.

[21] T. Kleine, K. Mezger, C. Münker, H. Palme, A. Bischoff, ^{182}Hf - ^{182}W isotope systematics of chondrites, eucrites, and martian meteorites: chronology of core formation and early mantle differentiation in Vesta and Mars, Geochimica et Cosmochimica Acta 68 (2004) 2935–2946.

[22] H. Samuel, P. Tackley, M. Evonuk, Heat partitioning during core formation by negative diapirism in terrestrial planets, Earth and Planetary Science Letters 290 (2010) 13–19.

[23] V. S. Solomatov, Origin of the Earth and Moon, University of Arizona Press, 2000, Ch. Fluid dynamics of a terrestrial magma ocean.

[24] E. Villermaux, B. Bossa, Single-drop fragmentation determines size distribution of raindrops, Nature Physics 5 (2009) 697–702.

[25] D. C. Rubie, H. Melosh, J. Reid, C. Liebske, K. Righter, Mechanisms of metal-silicate equilibration in the terrestrial magma ocean, Earth and Planetary Science Letters 205 (2003) 239–255.

[26] T. W. Dahl, D. J. Stevenson, Turbulent mixing of metal and silicate during planet accretion and interpretation of the Hf-W chronometer, Earth and Planetary Science Letters 295 (2010) 177–186.

[27] R. Deguen, P. Olson, P. Cardin, Experiments on turbulent metal-silicate mixing in a magma ocean, Earth and Planetary Science Letters 310 (2011) 303–313.

[28] M. Ulvrová, N. Coltice, Y. Ricard, S. Labrosse, F. Dubuffet, J. Velimský, O. Srámek, Compositional and thermal equilibration of particles, drops, and diapirs in geophysical flows, Geochemistry Geophysics Geosystems 12 (2011) 1–11.

[29] R. Deguen, M. Landeau, P. Olson, Turbulent metal-silicate mixing, fragmentation, and equilibration in magma oceans, Accepted for publication in 2013.

[30] H. Ichikawa, S. Labrosse, K. Kurita, Direct numerical simulation of an iron rain in the magma ocean, Journal of Geophysical Research 115 (2010) B01404.

[31] S.-I. Karato, V. Murthy, Core formation and chemical equilibrium in the Earth- I. physical considerations, Physics of the Earth and Planetary Interiors 100 (1997) 61–79.

[32] T. Bonometti, J. Magnaudet, Transition from spherical cap to toroidal bubbles, Physics of Fluids 18 (2006) 052102.

[33] M. Ohta, S. Yamaguchi, Y. Yoshida, M. Sussman, The sensitivity of drop motion due to the density and viscosity ratio, Physics of Fluids 22 (2010) 072102.